Anthropogenic impacts on changes in summer extreme precipitation over China during 1961–2014: roles of greenhouse gases and anthropogenic aerosols

Anthropogenic impacts on changes in summer extreme precipitation over China during 1961-2014: roles of greenhouse gases and anthropogenic aerosols

Yan Guo[1*], Buwen Dong[2], Jiangshan Zhu[3]

1. *State Key Laboratory of Earth Surface Processes and Resource Ecology, Beijing Normal University, Beijing 100875, China*
2. *National Centre for Atmospheric Science, Department of Meteorology, University of Reading, Reading, UK*
3. *Institute of Atmospheric Physics, Chinese Academy of Sciences, Beijing 100029, China*

*Corresponding author: Yan Guo (guoyan@bnu.edu.cn)

Abstract

Extreme precipitation often causes enormous economic losses and severe disasters. Changes in extreme precipitation potentially have large impacts on the human society. In this study, we investigated the changes in four precipitation extreme indices over China during 1961~2014. The indices include total wet-day precipitation (PRCPTOT), precipitation on extremely wet days (R95pTOT), number of extremely wet days (R95d) and precipitation intensity on extremely wet days (R95int) during the extended summer (May-August). Observation analyses showed that these four indices have significantly increased over southeast China (SEC) and northwest China (NWC) whilst decreased over northeast China (NEC) and southwest China (SWC). Based on HadGEM3-GC3.1 historical, greenhouse gas only (GHG) and anthropogenic aerosol only (AA) simulations, we assessed the relative roles of different forcings in the observed trends. Model reproduced the main features of increasing trends over SEC and NWC in historical simulations, suggesting a dominant role of forced changes in the trends of four indices over the two regions. Individual forcing simulations indicated that GHG and AA forcings influence the increases in summer extreme precipitation over SEC and NWC, respectively, through different processes. Over SEC, extreme precipitation increase is mainly due to GHG forcing that results in moisture flux convergence increase through thermodynamic and dynamic effects. In comparison to GHG forcing, AA forcing has a weak contribution because AA forced moisture flux convergence increase is offset by AA forced evaporation reduction. Over NWC, extreme precipitation increase is primarily attributed to AA forcing and secondarily to GHG forcing. AA forcing can result in moisture flux convergence increase through dynamic effect, and GHG forcing can result in evaporation increase.

Key words summer extreme precipitation, anthropogenic impact, greenhouse gases, aerosols, China

1. Introduction

Increased frequency and intensity of extreme precipitation have been observed in the context of global warming, which have prominent impacts on the human society, ecosystems, and environment (IPCC, 2021). Extreme precipitation often causes enormous economic losses and severe disasters. East China has experienced significant increases in extreme precipitation during the last few decades (Zhou et al. 2016), which cause enormous economic losses due to locally high population density and rapid economic development. For example, the annual economic losses caused by floods increased from 80.2 billion Yuan during 1984~2003 to 122.83 billion Yuan during 2004~2013 over China (Qin et al., 2015). Therefore, understanding the causes for changes in extreme precipitation over China and providing reliable projection of future changes are of great significance, which are particularly concerned by both scientific community and decision makers.

Human-induced increases in greenhouse gases (GHGs) have contributed to the observed intensification of extreme precipitation over many land areas (Min et al. 2011; Zhang et al. 2013, Dong et al. 2020, 2021). GHG impacts have been detected over China both on the increasing trend of precipitation extremes (Chen and Sun 2017; Li et al. 2017; Lu et al. 2020) and individual heaviest precipitation events (Sun et al. 2019). Physically, GHG induced global warming could enhance atmospheric water holding capacity, favoring more heavy precipitation. Meanwhile, GHG induced modulation of the East Asian summer monsoon (EASM) circulation can give rise to more moisture flux convergence over east China, favorable to more heavy precipitation (Ma et al. 2017). It was demonstrated that under GHG forcing, EASM circulation can be modulated through intensified land-ocean thermal contrast as well as uneven warming of sea surface temperature (SST) that resulted in intensified western North Pacific subtropical high (WNPSH) via strengthened local Hadley circulation (Tian et al. 2018) or weakened Walker circulation (Lin et al. 2020).

In addition to GHGs, increases in anthropogenic aerosol (AA) emissions have essential influences on precipitation changes, although its influences are complex that includes direct (aerosol radiation interaction) and indirect impacts (aerosol cloud interaction). By scattering and absorbing solar radiation, aerosols can prevent the shortwave radiation reaching the earth surface, termed as aerosol radiation interaction. By directly interacting with cloud, aerosols can change cloud radiation properties and

precipitation efficiency, termed as aerosol cloud interaction (Dong et al. 2019). Besides direct interaction with cloud through microphysical processes to affect precipitation, aerosols have the potential to affect circulation through altering radiation budget. AAs have been demonstrated to play an important role for the observed weakening of the EASM circulation (Dong et al. 2019; Song et al. 2014; Tian et al. 2018) and the reduced summer extreme precipitation over north China (Lin et al. 2018; Zhang et al. 2017). Ma et al. (2017) showed evidences that AA could partially offset the GHG induced increases in heavy precipitation over east China.

Although previous studies have investigated the anthropogenic influences on precipitation changes over China, a few studies focused on the changes in extreme precipitation defined by percentile-based extreme indices, and the exact physical mechanism underlying are still not clear. In this study, our main aim is to elucidate the relative roles of GHG forcing and AA forcing on the changes in summer extreme precipitation over China, and to understand the physical processes responsible. We use a set of experiments based on a state-of-the-art climate model HadGEM3 in the Global Coupled configure (HadGEM3-GC3.1) that participates in the sixth phase of Coupled Model Inter-comparison Project (CMIP6) (e.g., Eyring et al., 2016; Gillett et al., 2016) to address these above questions.

The structure of this paper is designed as follows: Sect.2 introduces the observational data, model and methodology. Sect.3 illustrates the observed changes in summer precipitation extremes over China. Sect.4 elucidates the anthropogenic roles including GHG forcing and AA forcing in shaping these changes and analyzes the related physical processes. Sect.5 and Sect.6 reveal the detailed physical mechanism in response to GHG forcing and AA forcing, respectively. Finally, our conclusion and discussion are summarized in Sect.7.

2. Observational data, model and methodology

As a reference from observation, gridded daily precipitation data with a spatial resolution of 1°×1° since 1961 were obtained from the CN05.1 dataset (Wu and Gao 2013). The CN05.1 dataset is produced by the National Climate Centre of the China Meteorological Administration from more than 2400 observational stations covering all of mainland China. The reliability of this dataset has been widely confirmed by previous research focused on climate over China (Luo et al., 2021; Zhou et al. 2016).

HadGEM3-GC3.1 represents the UK's contribution to the CMIP6 (e.g., Andrews

et al., 2020). This physical climate model consists of global atmosphere-land configuration GA7/GL7.1, the global ocean GO6 and the sea ice model configuration GSI8.1, coupled with the OASIS-MCT coupler. Its lower resolution configuration was used in this study, which has a nominal atmospheric resolution of 135 km (85 levels) and an ocean resolution of 1° (75 levels) with coupling every 3 hours. Three types of experiment designed in CMIP6 were employed, which are (1) historical simulations with all external forcings (All) including external anthropogenic forcings (GHGs, AAs, ozone, and land use) and external natural forcings (solar and volcanic activities); (2) GHG-only simulations (GHG) forced by GHGs only; (3) AA-only simulations (AA) forced by AAs only (e.g., Eyring et al., 2016; Gillett et al., 2016). A common period 1961~2014 among three experiments were concerned. All five ensemble members r1i1p1f3~r5i1p1f3 were used. Ensemble mean of five ensemble members was used to represent the external forced responses.

Changes of extreme precipitation during the boreal extended summer from May to August were studied. Four precipitation extreme indices were used which are defined according to the approach recommended by the Expert Team on Climate Change Detection and Indices (ETCCDI), i.e., total wet-day precipitation (PRCPTOT, unit: mm), precipitation on extremely wet days (R95pTOT, unit: mm), number of extremely wet days (R95d, unit: days), precipitation intensity on extremely wet days (R95int, unit: mm/day). A wet day was defined as daily precipitation $\geq$ 1 mm. An extremely wet day was defined as daily precipitation > the 95th percentile of daily precipitation on wet days over the base period 1961~1990 in the boreal extended summer. We used linear trend to describe the long-term change, which is estimated using the least square method and its statistical significance is tested using a two-tailed Student's t-test.

3. Observed changes in summer precipitation extremes

Figure 1 shows the observed trends of summer wet-day total amount (PRCPTOT), extremely wet-day amount (R95pTOT), extremely wet-day frequency (R95d), and extremely wet-day intensity (R95int) during 1961~2014 (54 years as 54a). Changes in PRCPTOT, R95pTOT, and R95int are expressed as percentage relative to the climatology over 1961~1990. Patterns of trends in these four extreme indices show a common feature, which is increase over the southeast and northwest China whilst decrease over the northeast and southwest China. Changes in both extreme precipitation frequency and intensity are in agreement with extreme precipitation amount, suggesting

that more extreme precipitation events occur over the southeast and northwest China with strengthened intensity, and oppositely less extreme precipitation events occur over the northeast and southwest China with weakened intensity.

To facilitate quantitative depiction, whole China was divided into four sub-regions, i.e., southeast China (SEC), northeast China (NEC), northwest China (NWC), and southwest China (SWC) as shown in Fig.1. The trends of regional averaged extreme indices were calculated over these four regions and shown in Fig.2 (white bar). Over SEC, PRCPTOT has increased at 8.8%/54a and R95pTOT has increased at 25%/54a. Responsible for the R95pTOT increase, R95d and R95int have consistently risen with rates of 0.7 days/54a and 7.4%/54a respectively. Similarly, significantly increasing trends are seen over NWC in the four extreme indices, which are 15.4%/54a in PRCPTOT, 34%/54a in R95pTOT, 0.8 days/54a in R95d, and 15.1%/54a in R95int. Contrary to the increases of precipitation extremes over SEC and NWC, precipitation extremes decreases are observed over NEC and SWC, not significant though.

4. Model simulated changes in precipitation extremes and related processes in response to different forcings

To understand the underlying drivers for the observed changes in precipitation extremes and the physical mechanism involved, a set of simulations based on HadGEM3-GC3.1 were analyzed. Figure 3a-3d are the simulated trends of four extreme indices in response to All forcing. Overall, model is able to reproduce precipitation extremes increases over SEC and NWC. This is consistent among five ensemble members. The simulated trends over SEC are 22.7±6.7%/54a in R95pTOT, 0.5±0.16 days/54a in R95d, and 6.4±2.9%/54a in R95int (blue bars in Fig.2), being very close to observation. The simulated trends over NWC are 15.1±6.4%/54a in R95pTOT, 0.3± 0.17 days/54a in R95d, and 7.6±5.6%/54a in R95int (blue bars in Fig.2), being underestimated to some extent but still significant. Above results suggest a dominant role of forced changes in the recent trends of extreme indices over the two regions. Observed decreases of precipitation extremes over NEC and SWC are not reproduced by model ensemble mean, as demonstrated by opposite trends against observation. The associated possible reasons will be discussed later. In the following, we will explore the detailed processes associated with the changes in summer precipitation extremes

198 just over SEC and NWC, rather than over all China, based on model HadGEM3-GC3.1.

199 To explore the anthropogenic effects on the changes in summer precipitation
200 extremes over SEC and NWC, the simulated trends in four extreme indices in response
201 to GHG forcing and AA forcing are respectively shown in Fig.3e-3h and Fig.3i-3l.
202 GHG forced pattern, resembling that in response to All forcing, is characterized by
203 prominent increases over the Yangtze-Huai River Basin and northwest China. AA
204 forced pattern shows a meridional dipole feature characterized by decrease over the
205 Yangtze River as well as its southern region and increase over northern China.

206 Trends of regional averaged extreme indices over SEC and NWC in response to
207 individual GHG forcing and AA forcing are shown in Fig. 2 (gray and green bars). Over
208 SEC, prominent increase of precipitation extremes are provided in response to GHG
209 forcing with trends of 29.9±6%/54a in R95pTOT, 0.9±0.26 days/54a in R95d, and 8.6
210 ±3.8%/54a in R95int, being consistent with those in response to All forcing. In contrast,
211 decrease of precipitation extremes are provided in response to AA forcing with trends
212 of –3.4±12.8%/54a in R95pTOT, –0.07±0.38 days/54a in R95d, and –3.8±2.7%/54a in
213 R95int. These results imply that model simulated increase of summer precipitation
214 extremes over SEC is predominantly due to GHG forcing, rather than AA forcing.
215 Unlike over SEC, model provided increased precipitation extremes over NWC in
216 response to both GHG forcing and AA forcing with trends of 11.5±4.8%/54a and 6.1±
217 8%/54a in R95pTOT, 0.2±0.05 days/54a and 0.13±0.13 days/54a in R95d, and 3.8±
218 3.7%/54a and 4.9±4.8%/54a in R95int, indicating that model simulated increase of
219 summer precipitation extremes over NWC is due to both GHG forcing and AA forcing.

220 As we know that global warming increases the water holding capacity of the
221 atmosphere, thus mean precipitation is expected to increase, and precipitation
222 characteristics are expected to change. A significant shift in probability distribution
223 functions (PDFs) of tropical precipitation toward intense rain have been expected
224 (Trenberth et al. 2003) and also widely observed (Lau et al. 2007). Ma et al. (2017) also
225 indicated this shift in PDFs of summer precipitation over East China. Increased mean
226 precipitation is contributed by increased extreme precipitation, suggesting an
227 association of increases between the mean precipitation and extreme precipitation,

although their increasing rate are different. In our study, changes in mean precipitation and precipitation extremes are in agreement with each other. As Fig.1 shows, the pattern of trend in PRCPTOT resembles those in R95pTOT, R95d and R95int with pattern correlation coefficients of 0.76, 0.54 and 0.6, respectively. And these associations are well represented in model. The pattern correlation coefficients of trend in PRCPTOT with that in R95pTOT, R95d and R95int are 0.84, 0.71, and 0.62 respectively in historical simulation. Mean precipitation increase usually exhibits extreme precipitation increase, therefore understanding the mechanisms responsible for mean precipitation increase will help us to understand that for extreme precipitation increase.

To investigate what processes contribute to the increases of summer precipitation over SEC and NWC, atmospheric moisture budgets have been examined. According to moisture budget equation, precipitation is balanced by evaporation and vertically integrated atmospheric moisture flux convergence at monthly or longer time scale (Trenberth and Guillemot 1995). Furthermore, the moisture flux convergence is decomposed into the dynamic component due to circulation changes and the thermodynamic component due to specific humidity changes, to facilitate studying the dynamic and thermodynamic effects (Li et al. 2015).

Figure 4 is the spatial pattern of trend in summer precipitation, evaporation, moisture flux convergence, and thermodynamic and dynamic components of moisture flux convergence in response to All forcing, GHG forcing, and AA forcing, respectively. Changes in precipitation (Fig. 4a-4c), evaporation (Fig. 4d-4f), and moisture flux convergence (Fig. 4g-4i) are compared. The similarity between changes in precipitation and moisture flux convergence indicates that moisture flux convergence change is predominantly responsible for precipitation change. Furthermore, the moisture flux convergence is decomposed into thermodynamic component (Fig. 4j-4l) and dynamic component (Fig. 4m-4o). The decomposition manifests that the pattern and magnitude of moisture flux convergence changes are mainly due to dynamic effect. Over SEC, thermodynamic effect also plays a role in response to All forcing (Fig. 4j) or GHG forcing (Fig. 4k), however it weakens dynamic effect in response to AA forcing (Fig. 4l).

To quantify the impacts of different forcings on extreme precipitation changes over SEC and NWC via distinctive physical processes, the trends of regional averaged summer precipitation, evaporation, moisture flux convergence, thermodynamic and

dynamic components over SEC and NWC are respectively shown in Fig. 5. Over SEC, summer precipitation increase in response to All forcing (blue bar) is attributed to moisture flux convergence increase that is further caused by both dynamic (62%) and thermodynamic (46%) effects. Isolating the roles of GHG forcing and AA forcing demonstrates that precipitation increase over SEC is due to GHG forcing (gray bar). The GHG forced precipitation increase is dominated by moisture flux convergence increase (95%) that is further caused by both thermodynamic (48%) and dynamic (49%) effects. Differently, AA forced (green bar) moisture flux convergence increase is offset by evaporation reduction. Moreover, moisture flux convergence increase is due to dynamic effect (148%), rather than thermodynamic effect that contributes negatively (–46%).

Over NWC, summer precipitation increase in response to All forcing (blue bar) is attributed to increases in both evaporation (61%) and moisture flux convergence (72%). The increase in moisture flux convergence is due to dynamic effect (158%). Isolating the roles of GHG forcing and AA forcing demonstrates that precipitation increase over NWC is primarily attributed to AA forcing (green bar), and secondarily to GHG forcing (gray bar). AA forced precipitation increase is dominated by the moisture flux convergence increase (83%) that is mainly caused by dynamic effect (144%), while GHG forced precipitation increase is mainly from evaporation increase (100%).

5. Mechanism related to GHG forcing

As shown in Sect. 4, model simulated summer precipitation increase over SEC is resulted from moisture flux convergence increase that is caused by both thermodynamic effect due to humidity increase and dynamic effect owing to strengthened circulation convergence. What detailed processes are responsible for the changes in humidity and circulation?

As air temperature increases in response to rising GHG concentration, atmosphere can hold more moisture, as demonstrated by increased vertically integrated precipitable water over SEC (Fig. 6a), which favors precipitation increase. Additionally, in response to GHG forcing, the enhanced WNPSH leads to anomalous southwesterly winds prevailing over SEC (Fig. 6b) that transport more moisture from the Bay of Bengal and the South China Sea and converge over the Yangtze-Huai River Basin (Fig. 4h), giving rise to local precipitation increase. These results basically agree with the results based on a specific model (MetUM-GOML2) with experiment design in

previous studies (Lin et al. 2020; Luo et al. 2019; Tian et al. 2018).

How does the WNPSH strengthen in response to GHG forcing? GHG forced SST changes show an El Nino-like SSTA (Fig. 6c), which is formed because the mixed layer depth is deeper over the western tropical Pacific than the eastern tropical Pacific, in turn, GHG forced warming is weaker over the west than the east. This mechanism has been indicated in the previous research (Collins et al. 2010). The zonal asymmetry of SST increase could weaken the Walker circulation (Fig. 6d), resulting in anomalous descent over the northwest Pacific and the enhanced WNPSH.

As indicated in Sect.4, GHG forced summer precipitation increase over NWC is mainly due to evaporation increase. What detailed process is responsible for the evaporation increase? Peng and Zhou (2017) investigated the summer precipitation increase over northwest China with reanalysis data, and they indicated that more than 50% of the increase is balanced by evaporation increase. The increased evaporation is favored by increased net surface radiation that is largely originated from the increased clear sky downward longwave radiation. According to their conclusion, the change in clear sky surface downward longwave radiation under GHG forcing is examined (Fig. 6e). Responding to GHG forcing, clear sky downward longwave radiation increases over all China, especially over northwest China and east China, which is responsible for the evaporation increase over there.

6. Mechanism related to AA forcing

As indicated in Sect.4, summer precipitation has not significantly changed over SEC in response to AA forcing, because the moisture flux convergence increase is offset by the evaporation reduction. Unlike over SEC, AA forced precipitation increases over NWC. It is resulted from moisture flux convergence increase, which is caused by dynamic effect due to strengthened circulation convergence. Detailed processes responsible for these changes are investigated in the following.

As indicated in previous research (Peng and Zhou 2017) that evaporation change is highly associated with net surface radiation change over NWC under GHG forcing, this association is demonstrated to exist over SEC in response to AA forcing (with correlation coefficient > 0.8). As AA emission increases over SEC, the downward shortwave radiation will reduce owing to aerosol radiation interaction and aerosol cloud interaction, which leads to net surface radiation reduction (Fig.7a) and finally evaporation reduction over SEC. Additionally, as air temperature drops due to AA

radiation effect, atmospheric capability to hold moisture will weaken, as demonstrated by reduced vertically integrated precipitable water (Fig.7b), which is also unfavorable for the precipitation over SEC.

Considering the anomalous circulation in response to AA forcing, the strengthened WNPSH results in anomalous southwesterly winds transporting moisture from the South China Sea to the SEC. These anomalous southwesterlies further flow northwestward after crossing the Huai River and converge over the NWC (Fig. 7c). These anomalous circulations cause moisture flux convergence increase over both the Yangtze-Huai River Basin and eastern part of NWC (Fig.4i), favorable for local precipitation increase.

Firstly, what drives those anomalous circulations? In AA forcing experiment, two high-value centers of sea level pressure anomaly (SLPA) are formed over north China and north India, respectively (Fig. 7c), which agree with local cooling anomalies (Fig. 7d) as AAs increase over there. In contrast, AAs are relatively low over the NWC, leading to relatively high air temperature anomaly (Fig. 7d) and relatively weak SLPA locally (Fig.7c). This spatial pattern of SLPA and associated zonal SLPA gradient between north China and NWC can lead anomalous southwesterlies to turn northwestward and become anomalous easterlies.

Secondly, how does the WNPSH strengthen in response to AA forcing? In Fig.7e (meridional section zonally averaged over 105°E~145°E), anomalous descent is found at about 20°N, which is responsible for the WNPSH strengthening, whilst its north (30°N~40°N) and south (0~10°N) sides are anomalous ascents. How does this anomalous meridional cell form over the northwest Pacific (NWP)? AA forced SST shows a tilted SSTA tripole pattern oriented in northwest-southeast direction lasting from the preceding winter to summer (Fig.8) with negative SSTA at about 20°N and positive SSTA on both northwest and southeast sides. This tilted SSTA tripole pattern and associated meridional SST gradient in pre-summer are responsible for the anomalous meridional cell shown in Fig.7e. This result is similar to the Fig.9 in Lin et al. (2020). As Lin et al. (2020) indicated, the anomalous cooling at about 20°N over NWP in pre-summer is highly associated with AA emissions that are advected from the East Asian continent by the prevailing winds.

To further understand why the meridional SSTA gradient disappears in the late summer (Fig.8d), we analyze the temporal evolution of zonally averaged (105°E~ 145° E) changes of SST, precipitation, total cloud amount and surface downward shortwave radiation related with cloud (Fig. 9). In Fig.9a, cooling SSTA at about 20°N is found to last from preceding winter until June. This cooling and its associated meridional SSTA gradient can drive meridional circulations. Its anomalous descending branch, located at about 20°N, can further depress the convection, suggesting reduced precipitation (Fig. 9b) and cloud amount (Fig. 9c). In turn, cloud reduction can increase the surface shortwave radiation (Fig. 9d) and warm the sea surface. This feedback associated with circulation, precipitation, cloud and surface radiation could mitigate the SSTA cooling, leading to weakened meridional SST gradient in the late summer (shown in Fig.8d).

7. **Conclusion and discussion**

In this study, we investigated the changes in four precipitation extreme indices over China during the extended summer over 1961~2014. Observation analyses show that these four extreme indices have significantly increased over SEC and NWC whilst decreased over NEC and SWC. Based on a CMIP6 model HadGEM3-GC3.1 historical, GHG and AA simulations, we investigated the impacts of anthropogenic forcing (including GHG and AA forcings) on these observed trends over SEC and NWC. Our main results are summarized as follows.

1. Model reproduced the main features of increasing trends over SEC and NWC in historical simulation, suggesting a dominant role of forced changes in summer precipitation extremes over these two regions. Individual forcing simulations indicated that GHG and AA forcings have influences on summer extreme precipitation increases over SEC and NWC, respectively, through different processes.
2. Over SEC, extreme precipitation increase is primarily due to GHG forced increase in moisture flux convergence that is caused by both thermodynamic and dynamic effects. In response to GHG forcing, atmosphere can hold more moisture as temperature increases, which is favorable to precipitation increase. In addition, GHG forced El Nino-like SSTA pattern can weaken the Walker circulation, resulting in enhanced WNPSH and its associated anomalous southwesterlies, which transport more moisture to SEC and converge, giving

rise to local precipitation increase. Different from GHG effect, AA forced circulation anomalies favor more moisture flux convergence over SEC but that is offset by AA forced local evaporation reduction due to reduced downward shortwave radiation. Thus, net effect of AA forcing has a weak contribution to precipitation increase over SEC.

3. Over NWC, extreme precipitation increase is primarily attributed to AA forced moisture flux convergence increase and secondarily to GHG forced evaporation increase. Spatially heterogeneous AA emissions result in anomalous zonal temperature gradient and SLP gradient between NWC and north China. The SLPA gradient can drive warm and wet southwesterlies to turn northwestward after crossing the Huai River and converge over NWC, which favor local precipitation increase. In response to GHG forcing, clear sky downward longwave radiation increased over NWC, leading to local evaporation increase, which is favorable to precipitation increase.

Our results are generally in agreement with previous studies of anthropogenic impacts on East Asian precipitation changes based on CMIP5 models (Ma et al. 2017; Zhou et al. 2020). Although the observed increases in summer precipitation extremes over NWC have been captured by model, the underestimation of trends are prominent (blue bar in Fig. 2). It is recognized that model bias exists, however the reliability of observational dataset over NWC needs to be concerned. CN05.1 dataset is produced from more than 2400 stations covering mainland China, but stations available in western China are sparse, especially over the Taklimakan desert in NWC (Wu and Gao 2013).

In addition, extreme precipitation changes over NEC and SWC have not further studied since model cannot reproduce the observed trends over these two regions in historical simulation. Simulation failure over SWC is possibly attributed to model bias due to complicated topography over there, which have been found to exist in many GCMs (Flato et al. 2013; Bao et al. 2015). While by comparison, the situation over NEC is different. From Fig.2 (blue bar) and Fig.3a-d, we found large inter-member spreads existing over NEC, which suggests that climate internal variability strongly influences, rather than external forcings, if perfect model is supposed. This issue whether summer extreme precipitation changes over NEC are dominated by internal variability deserves future investigation based on climate models with larger ensemble.

Acknowledgements

We acknowledge the international modeling groups for providing their data for analysis, the Program for Climate Model Diagnosis and Inter-comparison (PCMDI) for collecting and achieving the model data, the World Climate Research Programme's (WCRP's) Coupled Model Inter-comparison Project (CMIP) for organizing the model data analysis activity. This study is jointly supported by the National Key Research and Development Program of China (2020YFA0608201) and the NSFC project (41975078). BD is supported by the UK National Centre for Atmospheric Science, funded by the Natural Environment Research Council.

Data Availability Statements

The datasets generated and/or analyzed during the current study are available from the corresponding author on reasonable request.

References

Andrews, M. B., Ridley, J. K., Wood, R. A., Andrews, T., Blockley, E. W., Booth, B., Burke, E., Dittus, A. J., Florek, P., Gray, L. J., Haddad, S., Hermanson, L., Hodson, D., Hogan, E., Jones, G. S., Knight, J. R., Kuhlbrodt, T., Misios, S., Mizielinski, M. S., Ringer, M. A., Robson, J., and Sutton, R. T. 2020: Historical simulations with HadGEM3-GC3.1 for CMIP6, J. Adv. Model. Earth Syst., e2019MS001995, https://doi.org/10.1029/2019MS001995

Bao, J., J. Feng, and Y. Wang, 2015: Dynamical downscaling simulation and future projection of precipitation over China, J. Geophys. Res. Atmos., 120, 8227–8243. Chen, H., and J. Sun, 2017: Contribution of human influence to increased daily precipitation extremes over China. Geophys Res Lett, 44, 2436-2444.

Collins, M., and Coauthors, 2010: The impact of global warming on the tropical Pacific Ocean and El Niño. Nature Geoscience, 3, 391-397.

448 Dong, B., L. J. Wilcox, E. J. Highwood, and R. T. Sutton, 2019: Impacts of recent
449 decadal changes in Asian aerosols on the East Asian summer monsoon: roles of
450 aerosol–radiation and aerosol–cloud interactions. Clim Dyn, 53, 3235-3256.
451 Dong, S., Y. Sun, and C. Li, 2020: Detection of human influence on precipitation
452 extremes in Asia. J. Climate, 33, 5293–5304, https://doi.org/10.1175/JCLI-D-19-
453 0371.1.
454 Dong S, Sun Y, Li C, Zhang X, Min S, Kim Y (2021) Attribution of extreme
455 precipitation with updated observations and CMIP6 simulations. J Clim
456 34(3):871–881. https://doi.org/10.1175/jcli-d-19-1017.1
457 Eyring V, Bony S, Meehl GA, Senior CA, Stevens B, Stoufer RJ, Taylor KE (2016)
458 Overview of the coupled model intercomparison project phase 6 (CMIP6)
459 experimental design and organization. Geosci Model Dev 9:1937–1958.
460 https://doi.org/10.5194/ gmd-9-1937-2016
461 Flato, G., et al. (2013), Evaluation of climate models, in Climate Change 2013: The
462 Physical Science Basis. Contribution of Working Group I to the Fifth
463 Assessment Report of the Intergovernmental Panel on Climate Change,
464 Cambridge Univ. Press, Cambridge, U. K., and New York.
465 Gillett NP, Shiogama H, Funke B et al (2016) The detection and attribution model
466 intercomparison project (DAMIP v1.0) contribution to CMIP6. Geosci Model Dev
467 9:3685–3697
468 IPCC, 2021: Climate Change 2021: The Physical Science Basis. Contribution of
469 Working Group I to the Sixth Assessment Report of the Intergovernmental Panel
470 on Climate Change. Cambridge University Press, Cambridge, UK and New York,
471 NY, USA, in press.
472 Lau, K. M., and H. T. Wu, 2007: Detecting trends in tropical rainfall characteristics,

1979–2003. *Int. J. Climatol.*, **27**, 979–988.

Li, H., H. Chen, and H. Wang, 2017: Effects of anthropogenic activity emerging as intensified extreme precipitation over China. Journal of Geophysical Research: Atmospheres, 122, 6899-6914.

Li, X., M. Ting, C. Li, and N. Henderson, 2015: Mechanisms of Asian Summer Monsoon Changes in Response to Anthropogenic Forcing in CMIP5 Models %J Journal of Climate. J Climate, 28, 4107-4125.

Lin, L., Y. Xu, Z. Wang, C. Diao, W. Dong, and S.-P. Xie, 2018: Changes in Extreme Rainfall Over India and China Attributed to Regional Aerosol-Cloud Interaction During the Late 20th Century Rapid Industrialization. Geophys Res Lett, 45, 7857-7865.

Lin, Z., B. Dong, and Z. Wen, 2020: The effects of anthropogenic greenhouse gases and aerosols on the inter-decadal change of the South China Sea summer monsoon in the late twentieth century. Clim Dyn, 54, 3339-3354.

Lu, C., F. C. Lott, Y. Sun, P. A. Stott, and N. Christidis, 2020: Detectable Anthropogenic Influence on Changes in Summer Precipitation in China, J Climate, 33, 5357-5369.

Luo, F., B. Dong, F. Tian, and S. Li, 2019: Anthropogenically Forced Decadal Change of South Asian Summer Monsoon Across the Mid-1990s. Journal of Geophysical Research: Atmospheres, 124, 806-824.

Luo, N., Y. Guo, J. Chou, and Z. Gao: Added value of CMIP6 models over CMIP5 models in simulating the climatological precipitation extremes in China, International Journal of Climatology, 1-17, doi:10.1002/joc.7294.

Ma, S., and Coauthors, 2017: Detectable Anthropogenic Shift toward Heavy Precipitation over Eastern China. J Climate, 30, 1381-1396.

Min, S.-K., X. Zhang, F. W. Zwiers, and G. C. Hegerl, 2011: Human contribution to

more-intense precipitation extremes. Nature, 470, 378-381.

Peng, D., and T. Zhou, 2017: Why was the arid and semiarid northwest China getting wetter in the recent decades? Journal of Geophysical Research: Atmospheres, 122, 9060-9075.

Qin DH, Zhang JY, Shan CC, Song LC. 2015. China National Assessment Report on Risk Management and Adaptation of Climate Extremes and Disasters (Refined Edition). Science Press: Beijing, 124 pp.

Song, F., T. Zhou, and Y. Qian, 2014: Responses of East Asian summer monsoon to natural and anthropogenic forcings in the 17 latest CMIP5 models. Geophys Res Lett, 41, 596-603.

Sun, Y., S. Dong, T. Hu, X. Zhang, and P. Stott, 2019: Anthropogenic Influence on the Heaviest June Precipitation in Southeastern China since 1961, B Am Meteorol Soc, 100, S79-S83.

Tian, F., B. Dong, J. Robson, and R. Sutton, 2018: Forced decadal changes in the East Asian summer monsoon: the roles of greenhouse gases and anthropogenic aerosols. Clim Dyn, 51, 3699-3715.

Trenberth, K. E., and C. J. Guillemot, 1995: Evaluation of the Global Atmospheric Moisture Budget as Seen from Analyses, J Climate, 8, 2255-2272.

Trenberth, K. E., A. Dai, R. M. Rasmussen, and D. B. Parsons, 2003: The changing character of precipitation. Bull. Amer. Meteor. Soc., **84**, 1205–1218.

Wu, J., and X.-J. Gao, 2013: A gridded daily observation dataset over China region and comparison with the other datasets, Chinese J Geophysics, 56, 1102-1111 (in Chinese).

Zhang, L., P. Wu, and T. Zhou, 2017: Aerosol forcing of extreme summer drought over North China. Environmental Research Letters, 12, 034020.

523 Zhang, X., H. Wan, F. W. Zwiers, G. C. Hegerl, and S.-K. Min, 2013: Attributing
524 intensification of precipitation extremes to human influence, Geophys Res Lett,
525 40, 5252-5257.
526 Zhou, B., Y. Xu, J. Wu, S. Dong, and Y. Shi, 2016: Changes in temperature and
527 precipitation extreme indices over China: analysis of a high-resolution grid dataset,
528 International Journal of Climatology, 36, 1051-1066.
529 Zhou T, W Zhang, et al., 2020: The dynamic and thermodynamic processes dominating
530 thereduction of global land monsoon precipitation driven by anthropogenic
531 aerosols emission, Science China (Earth Sciences), 63, 919-933.
532

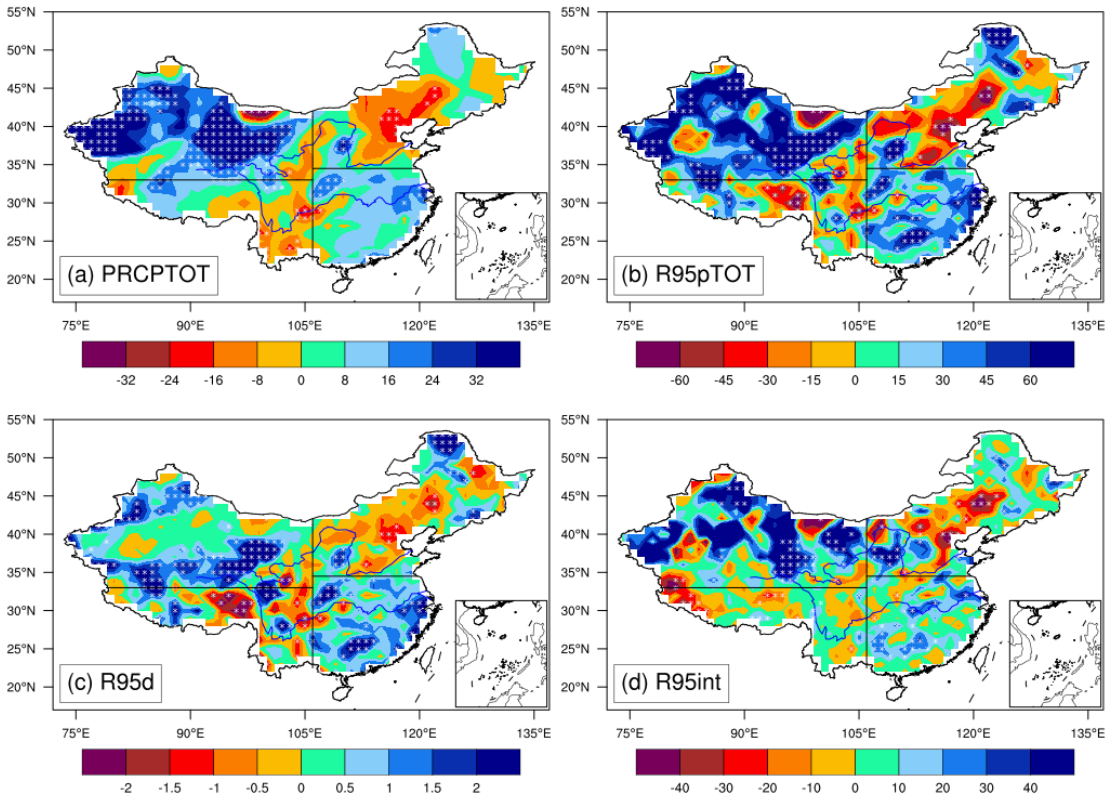

FIG.1 Observed linear trends in summer precipitation extremes during 1961~2014 (54 years as 54a): (a) PRCPTOT (%/54a), (b) R95pTOT (%/54a), (c) R95d (days/54a) and (d) R95int (%/54a). Changes in PRCPTOT, R95pTOT, and R95int are expressed as percentage relative to the climatologic mean over 1961~1990. The cross marks denote trends being statistically significant at the 90% confidence level using two-tailed Student's t-test. The straight lines divide China into southeast China (SEC), northeast China (NEC), northwest China (NWC) and southwest China (SWC) which are used for regional mean analysis.

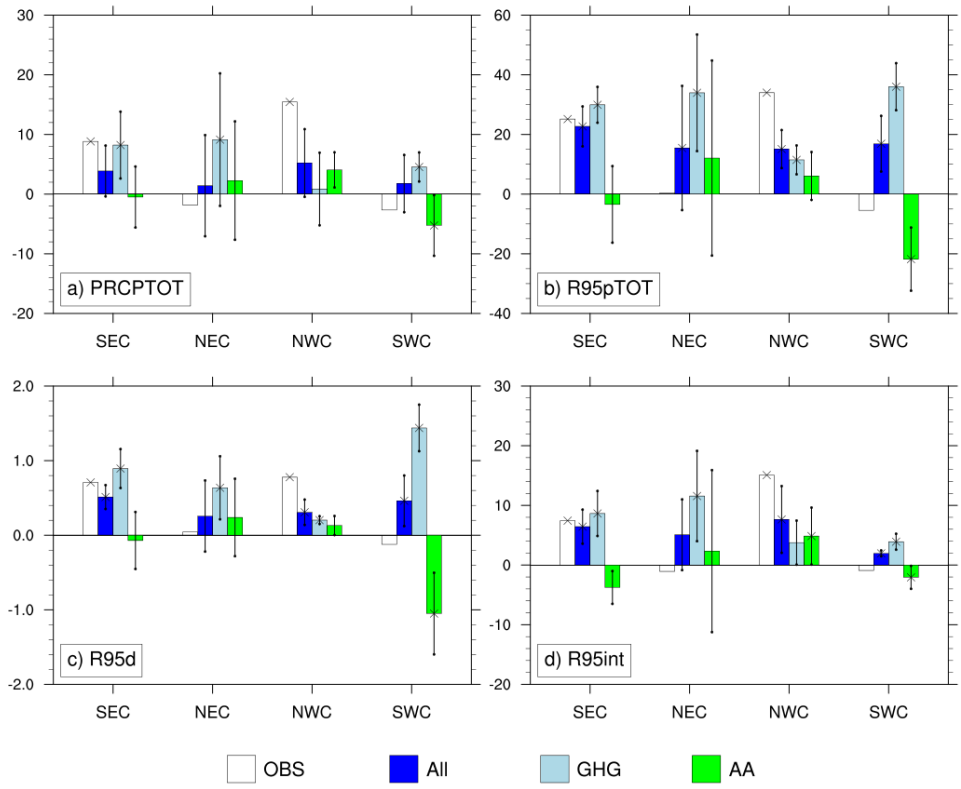

543

544 FIG. 2 Observed and model simulated linear trends of regional averaged summer
545 precipitation extremes during 1961~2014 in response to All forcing, GHG forcing and
546 AA forcing over southeast China (SEC), northeast China (NEC), northwest China
547 (NWC) and southwest China (SWC) (Fig. 1). Changes in PRCPTOT, R95pTOT, and
548 R95int are expressed as percentage relative to the climatologic mean over 1961~1990
549 with units of %/54a; unit for R95d is days/54a. The bars are ensemble mean; the dots
550 are ensemble mean±one standard deviation across five ensemble members; the cross
551 marks denote trends being statistically significant at the 90% confidence level using
552 two-tailed Student's t-test.

553

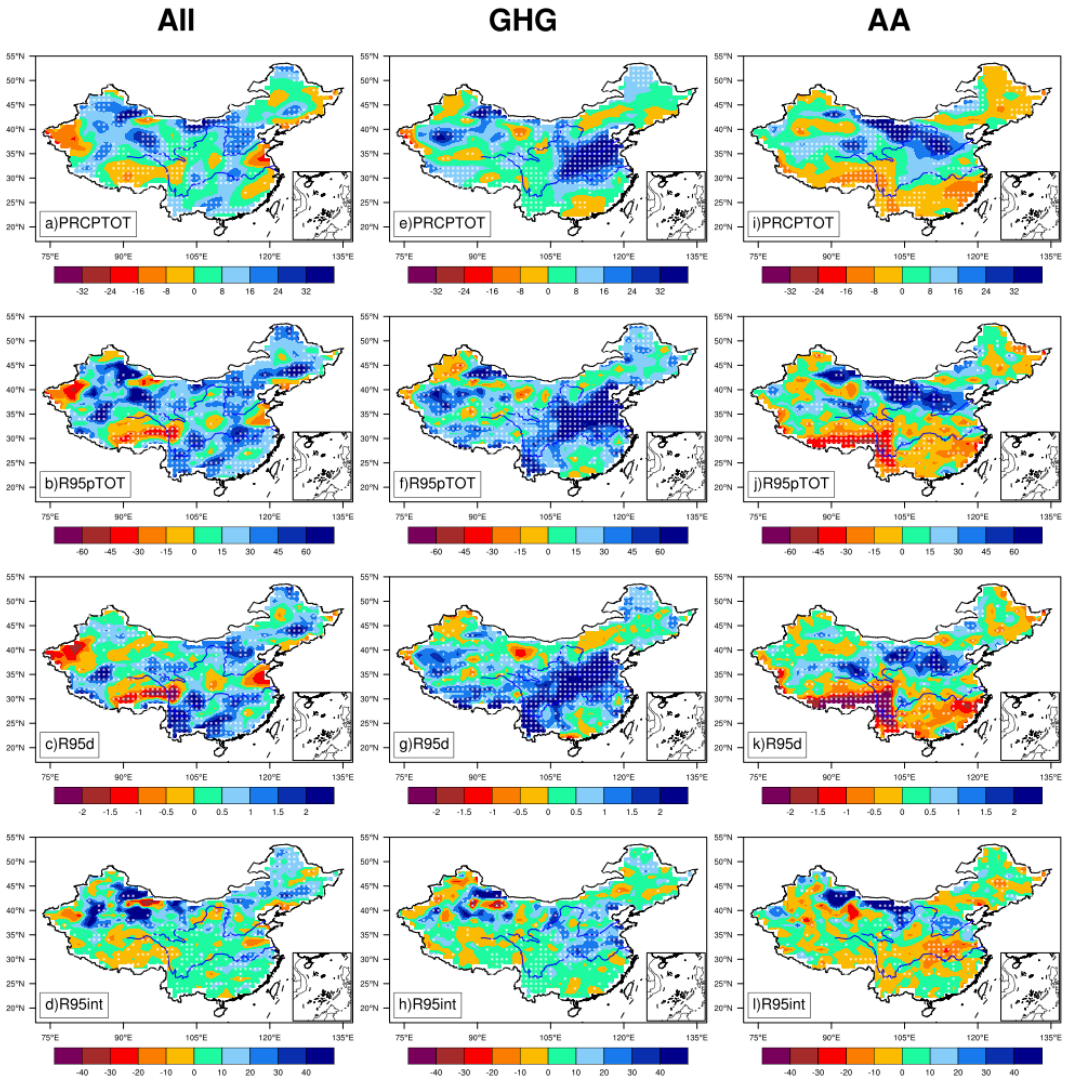

554

555 FIG. 3 Model simulated linear trends in summer PRCPTOT (%/54a), R95pTOT
556 (%/54a), R95d (days/54a), and R95int (%/54a) during 1961~ 2014 in response to (a-d)
557 All forcing, (e-h) GHG forcing, and (i-l) AA forcing. Changes in PRCPTOT, R95pTOT,
558 and R95int are expressed as percentage relative to the climatologic mean over
559 1961~1990.The shadings are ensemble mean; the cross marks denote signal-to-noise
560 ratio larger than 1 (signal: ensemble mean; noise: one standard deviation across five
561 ensemble members).

562

563

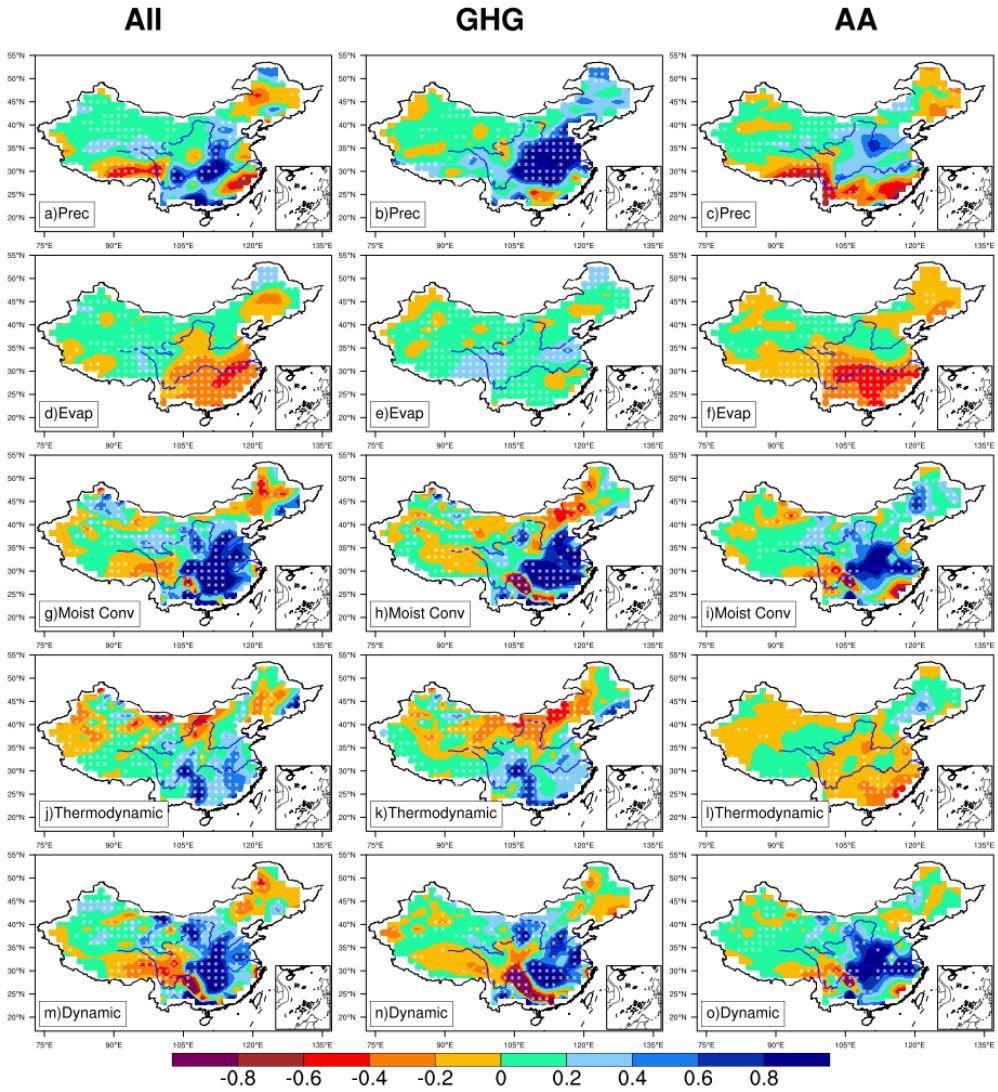

FIG.4 Model simulated linear trends in summer (a-c) total precipitation (mm day^{-1}/54a), (d-f) evaporation (mm day^{-1}/54a), (g-i) moisture flux convergence (mm day^{-1}/54a), (j-k) thermodynamic component (mm day^{-1}/54a), and (m-o) dynamic component (mm day^{-1}/54a) during 1961~2014 in response to All forcing, GHG forcing and AA forcing. The shadings are ensemble mean; the cross marks denote the signal-to-noise ratio larger than 1 (signal: ensemble mean; noise: one standard deviation across five ensemble members).

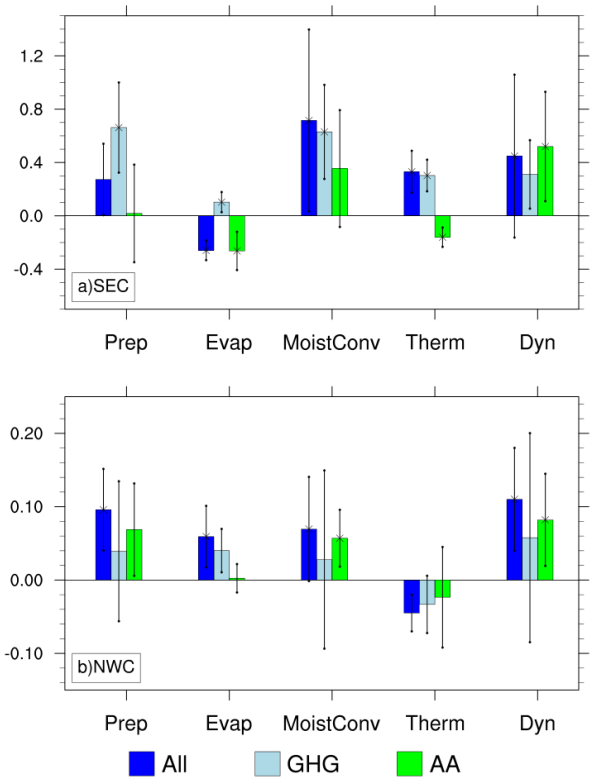

FIG.5 Model simulated linear trends in regional averaged summer precipitation (mm day^{-1}/54a), evaporation (mm day^{-1}/54a), moisture flux convergence (mm day^{-1}/54a), thermodynamic component (mm day^{-1}/54a) and dynamic component (mm day^{-1}/54a) during 1961~2014 in response to All forcing, GHG forcing and AA forcing over (a) southeast China and (b) northwest China. The bars are ensemble mean; the dots are ensemble mean±one standard deviation across five ensemble members; the cross marks denote trends being statistically significant at the 90% confidence level using two-tailed Student's t-test.

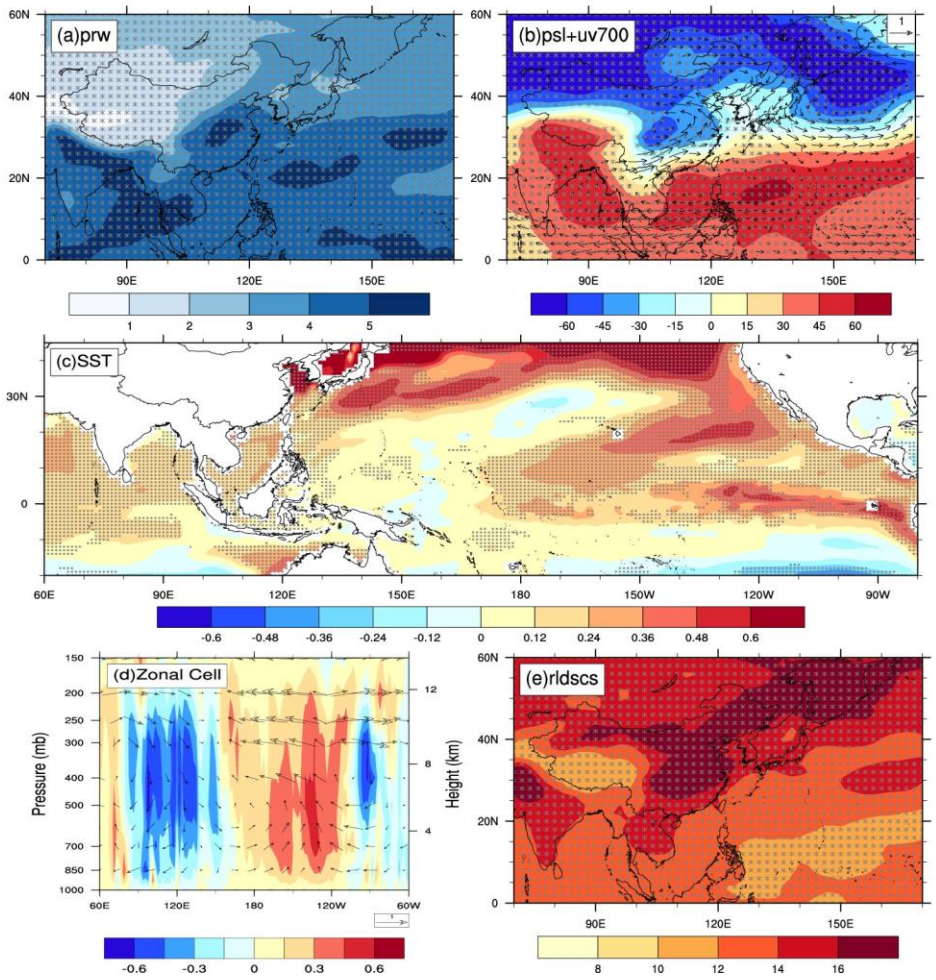

FIG.6 Model simulated (ensemble mean) linear trends during summer in response to GHG forcing. (a) Precipitable water (Kg m^{-2}/54a), (b) sea level pressure (shadings, Pa/54a) and 700hPa horizontal winds (vectors, m s^{-1}/54a), (c) sea surface temperature (°C/54a), (d) omega (shadings, Pa s^{-1}/54a) and omega-u vectors averaged over 5°S~20° N and (e) clear sky surface downward longwave radiation (W m^{-2}/54a). Omega is scaled to match the value of meridional wind and its sign is reversed. The cross marks denote the signal-to-noise ratio larger than 1 (signal: ensemble mean; noise: one standard deviation across five ensemble members).

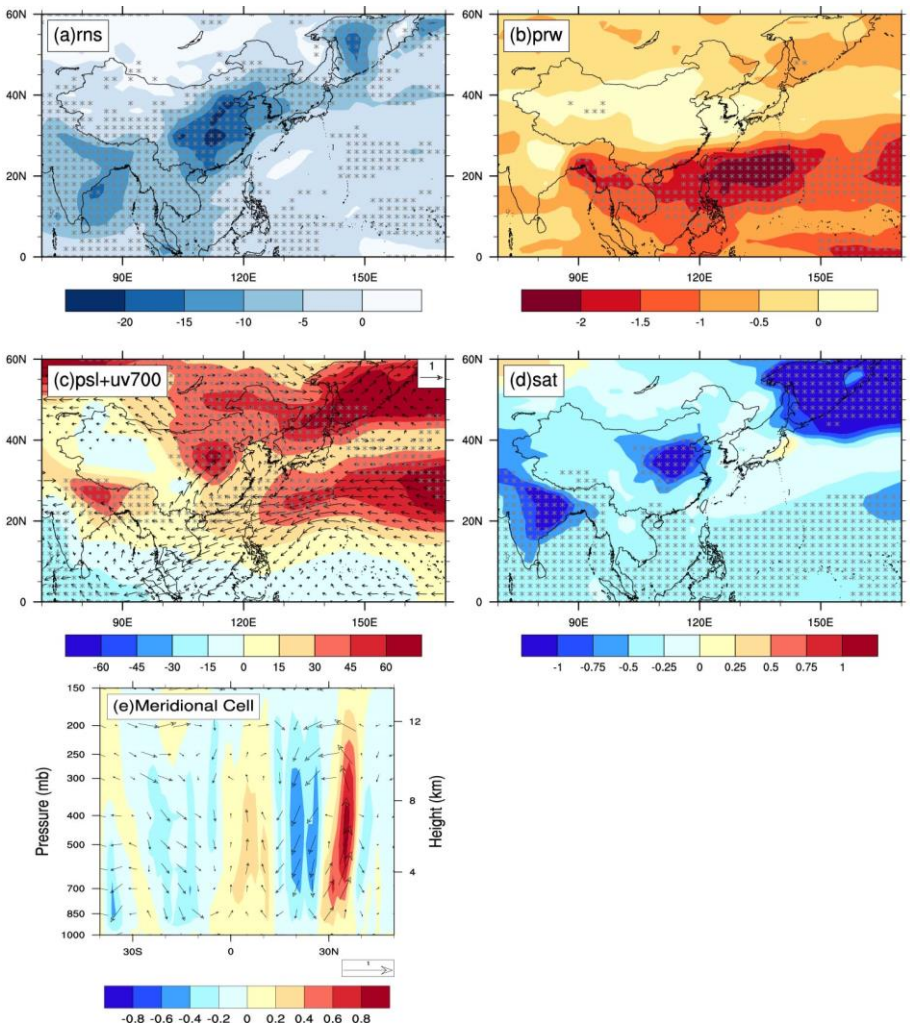

FIG.7 Model simulated (ensemble mean) linear trends during summer in response to AA forcing. (a) Net surface radiation (W m^{-2}/54a), (b) precipitable water (Kg m^{-2}/54a), (c) sea level pressure (shadings, Pa/54a) and 700hPa horizontal winds (vectors, m s^{-1}/54a), (d) near-surface air temperature (K/54a) and (e) omega (shadings, Pa s^{-1}/54a) and omega-v vectors averaged over 105°E ~145°E. Omega is scaled to match the value of meridional wind and its sign is reversed. The cross marks denote the signal-to-noise ratio larger than 1 (signal: ensemble mean; noise: one standard deviation across five ensemble members).

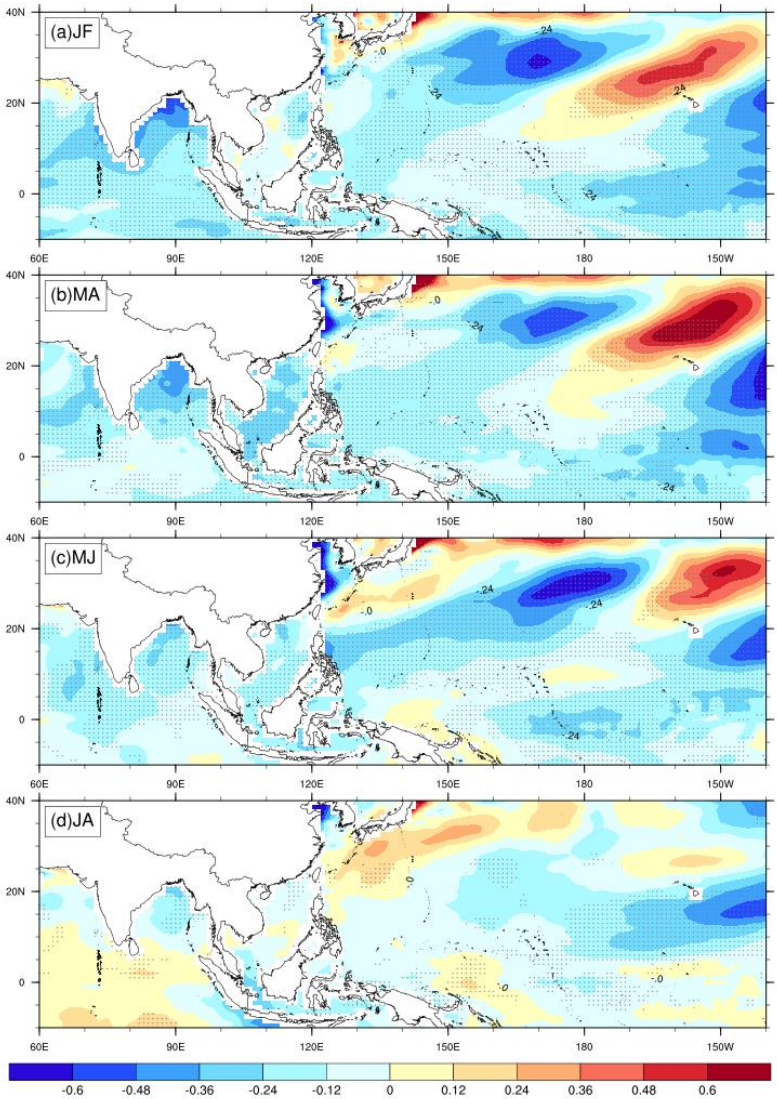

FIG. 8 Model simulated (ensemble mean) linear trends in sea surface temperature (℃/54a) in response to AA forcing from preceding winter to summer. The cross marks denote the signal-to-noise ratio larger than 1 (signal: ensemble mean; noise: one standard deviation across five ensemble members).

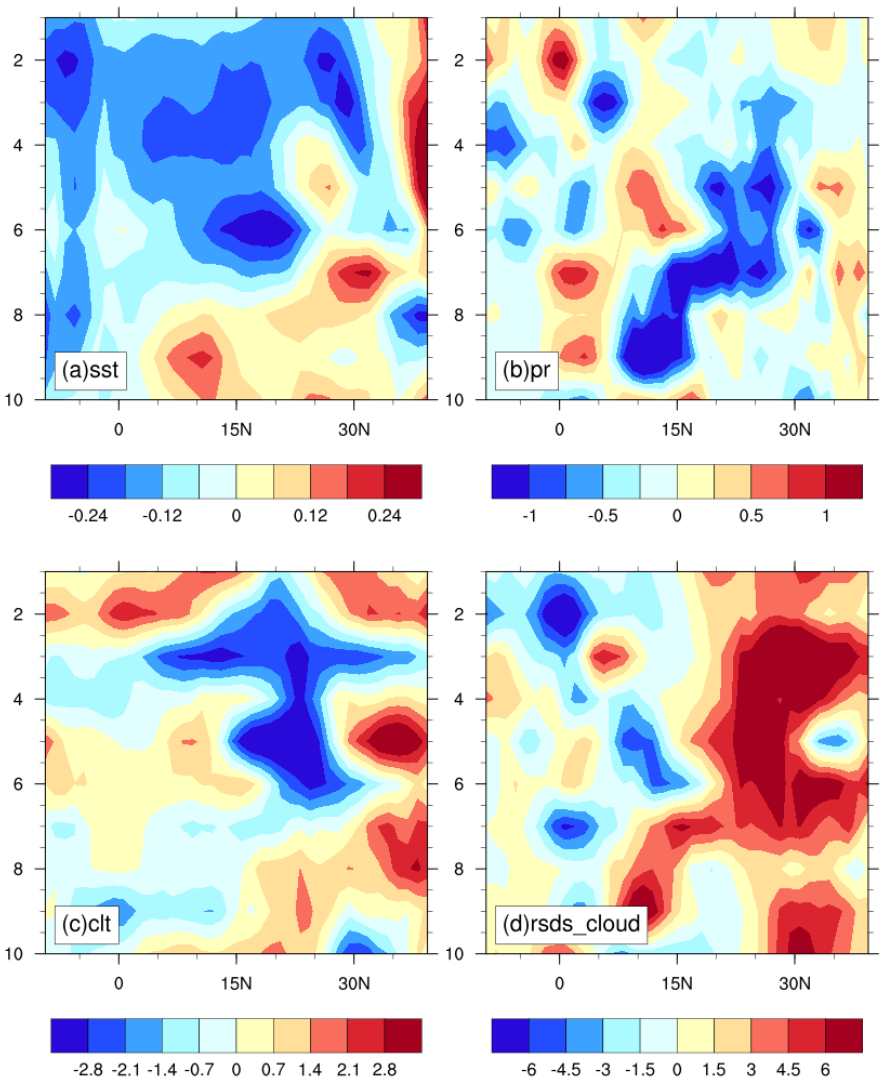

611

612 FIG.9 Evolution of model simulated (ensemble mean) linear trends averaged over 105°

613 E ~145°E from January to October in response to AA. (a) Sea surface temperature

614 (℃/54a), (b) precipitation (mm day^{-1}/54a), (c) total cloud amount (%/54a) and (d)

615 surface downward shortwave radiation related with cloud (W m^{-2}/54a).

616

617